Local Current Density and Electrochemical Impedance Measurements within 50 cm Single-Channel PEM Electrolysis Cell

C. Immerz, B. Bensmann, P. Trinke, M. Suermann, and R. Hanke-Rauschenbach

Institute of Electric Power Systems, Leibniz Universität Hannover, 30167 Hannover, Germany

The present analysis shows the local distribution of current density and EIS measurements along a 50 cm single-channel proton exchange membrane water electrolysis (PEMWE) cell. Measurements for operating modes with one sufficiently high and one insufficiently low stoichiometric water ratio (λ) were carried out to observe effects on the current density distribution. Furthermore, global and local EIS measurements were performed to distinguish between the cell voltage loss differences in the two cases. The mass transport losses η_{mtx} and the Ohmic voltage losses η_{Ω} show a strong increase, when the stoichiometric water ratio falls below a level of $\lambda \approx 5$. The reduction of the inlet water flux of the anode reduces both the proton conductivity of the ionomer within the catalyst layer and the membrane, increasing transport and Ohmic resistances, respectively. The local analysis has shown that the level of membrane and catalyst hydration under low stoichiometric conditions can be distributed highly non-homogeneous in along-the-channel direction, with the most pronounced dehydration toward the end of the channel.

 [DOI: 10.1149/2.0411816jes]

Manuscript submitted September 12, 2018; revised manuscript received November 6, 2018. Published December 12, 2018.

The characterization of locally distributed phenomena is widely used for proton exchange membrane fuel cells (PEMFCs). As first of its kind, Cleghorn et al.[1] combined the measurement of the current density distribution (CDD) with a local determination of the high frequency resistance to observe the effect of different flow and humidification rates on the local performance of a quadratic 100 cm^2 cell. Furthermore, spatially resolved current density mapping was used in PEMFCs to observe the effects of inhomogeneous catalyst distribution on the cell performance,[2] to evaluate catalyst gradients along the in-plane direction in order to compensate non-homogeneous CDDs due to temperature, hydration or mass flow effects[3,4] or to observe nonlinear pattern formation.[5,6]

However, the investigation of the in-plane CDD in proton exchange membrane water electrolysis (PEMWE) cells is a rather new topic. Verdin et al.[7] discussed the influence of contact pressure on the homogeneity of CDD. Experimental analyses with a 250 cm^2 circular and a 50 cm^2 square cell have shown that the contact pressure and the resulting interfacial contact resistances may result in heavily non-homogeneous CDDs, which can lead to local temperature hot-spots and consequently enhance local degradation processes. Other works from Sun et al.,[8] Dedigama et al.[9] and one own recent work[10] focused on the operating conditions and their effects on temperature distribution and in particular on the CDD along the channel coordinate.

Based on these works the present analysis gives a more detailed view on the water shortage in a segmented PEMWE cell with low stoichiometric water ratios, to investigate underlying performance losses. Currently, high water fluxes are state of the art to control temperature profiles easily,[11] which is feasible due to the low costs for the water circulation.[12] However, with favored higher current densities[13] and an objective to build PEMWE systems on a MW-level, lower stoichiometric water ratios may offer the potential for system optimization. Additionally, analyses at low stoichiometric water ratios widen the understanding of water transport paths inside the cell. Therefore, in the present work experiments were carried out, in which the CDD and the locally distributed cell impedance of a single-channel PEMWE cell were observed, to analyze the underlying processes.

Experimental

In the first subsection, the experimental cell setup and the segmentation of the cell are briefly described. The following subsection focuses on the electrical setup and the corresponding description of the measurement systems. Finally, the structure and function of the test station is explained.

Cell setup.—The experimental cell is a conventional setup of a PEMWE cell with a rectangular single channel geometry and an active area of 50.4 cm × 0.45 cm = 22.68 cm^2. The anode and cathode channels are 536 mm long and 1.5 mm wide. The anode channel is 2.0 mm deep, whereas the cathode channel has a depth of 0.5 mm. The special feature of this cell is its single-channel geometry, which represents a repeating unit within a single cell in a MW-PEMWE system.

Fig. 1a shows the channel coordinate and its segmentation along the channel, which is differently realized for each sandwich layer. The cell is segmented into three identical segments (length: 3.2 cm), in which local electrochemical impedance spectroscopy (EIS) measurements are performed, and four adjacent segments of different sizes. The dimensions and positions of these seven segments are shown scaled in Fig. 1a. The sandwich structure is presented in Fig. 1b. The top layer in the sandwich coordinate is the anode end plate made out of titanium. The anode end plate is separated into the seven segments by six grooves (each ≈ 2.0 mm wide) which are sealed with electrically insulating PTFE gaskets.

The underlying porous transport layer (PTL) is a titanium fiber material from Bekaert (2GDL40-1,00 thickness: 1.0 mm, porosity: 50%, fiber diameters: 25 µm and 40 µm). The PTL strip is 0.45 cm wide and also divided into seven segments. To fix the PTL stripes a frame of a highly compressible Gore (GR 15 (ePTFE)) gasket is used to prevent leakage of the cell and to insulate the particular segments electrically. On the cathode side the same Ti-PTLs and gaskets were used, to ensure a reasonable homogeneous contact pressure distribution.

A commercial catalyst coated membrane (CCM) from Ion Power was used in the current setup made from a Nafion117 membrane with IrO_x-based anode catalyst and Pt/C-based cathode catalyst. In contrast to the PTLs and the anode end plate, the catalyst layers are not segmented. Literature data has shown that in-plane currents are negligible under equipotential conditions.[14]

The cathode flow channel is milled in a plastic plate and framed by 252 current and temperature measurement shunts. Each measurement plate is electrically independent from its neighbors. Additionally, the cell has a thermal control system based on Peltier and electrical heating elements mounted on the cathode and anode end plates, respectively (not shown in Fig. 1). This enables the generation of a homogeneous temperature profile and an isothermal operation along the channel. A more detailed description of the cell is given in the authors' previous work.[10]

Measurement and test station setup.—The setup of the cathode end plate allows a 1-D observation of the CDD and the temperature

[z]E-mail: boris.bensmann@ifes.uni-hannover.de

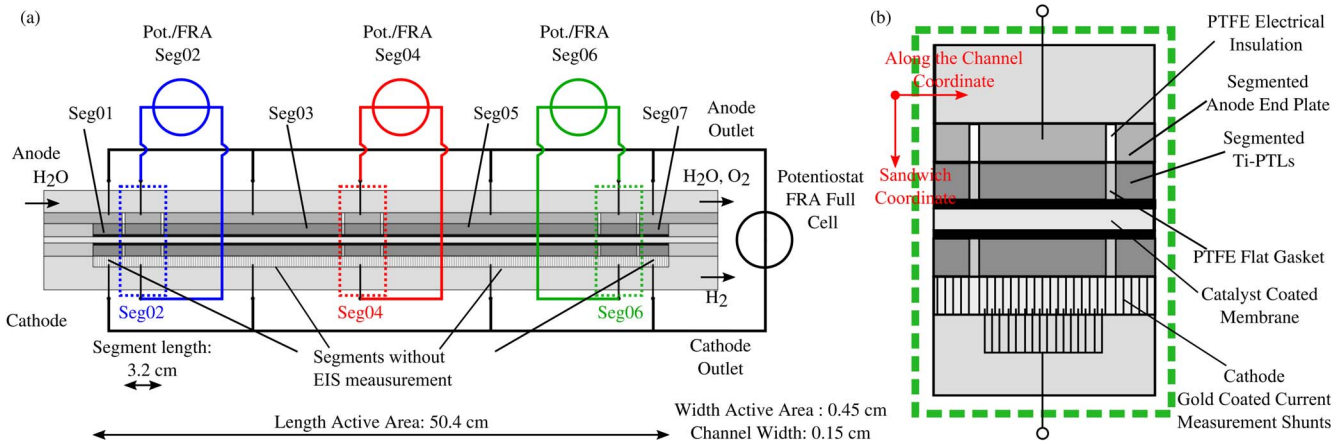

Figure 1. Schematic drawing of experimental setup: (a) 50 cm single-channel cell with the electrical contacting of the cell for a segmented electrochemical impedance spectroscopy (EIS) in segments Seg02, Seg04, Seg06. Neighboring segments Seg01, Seg03, Seg05 and Seg07 were not used for EIS measurements (b) Sandwich structure of one EIS measurement segment of the PEM electrolysis cell.

distribution. With 252 measurement plates (each 2.0 mm long) a very fine resolution was achieved. A printed circuit board from *S++* is used, in which shunt resistors measure the current and temperature of each gold coated measurement plate.

A more coarse, overlaying segmentation was used to perform local EIS. Therefore, 16 adjacent CDD segments are combined to one EIS segment, each at the inlet (Seg02), the middle (Seg04) and the outlet of the cell (Seg06) (compare with Fig. 1a for the segmentation and Fig. 1b for the combination of 16 CDD measurement plates to one EIS segment).

To perform EIS measurements for the integral cell, a Solartron ModuLab XM PSTAT together with a power booster (6 V/100 A) was used. The three segments for the EIS measurements and the residual segments are connected by wires of equal length to one connection point, at which the potentiostat with integrated frequency response analyzer is attached. This setup sets all segments to the identical potential and insulates them electrically.

For a local EIS measurement, the desired segment is separated from the anode and the cathode connecting points and directly attached to the Solartron unit and a power booster of reduced current range (20 V/2.0 A). Consequently, the certain segment is electrically insulated from the rest of the cell. The other segments are connected to a second DC power supply (HEIDEN HE-LAB/SMS). An identical cell voltage was adjusted for both electrical power supplies (potentostatic operation mode), to achieve a homogeneous potential distribution along the channel. Fig. 1a illustrates the electrical connection for a segmented EIS measurement at the segments Seg02, Seg04 and Seg06. The three EIS measurement segments were measured separately and consecutively, once steady state conditions were achieved.

As one alternative measurement setup, a serial connection of the three EIS measurement segments was taken into account. However, a compulsory voltage gradient from segment to segment would drive leaking currents in the in-plane direction of the unsegmented catalyst layer. Additionally, as a further alternative a parallel circuit of the three segments was considered. However, the implementation of three well-coordinated measurement shunts and the much higher effort for the data acquisition were estimated to be less efficient in contrast to a consecutive measurement. Therefore, both alternative measurement setups were not used in the herein analysis.

The experiments were performed with a simple in-house test station. The water flux on the anode side is controlled with a Coriolis flowmeter and a gear pump in a range of 0.1 g $min^{-1} \leq \dot{M}_{in}^{A} \leq$ 30 g min^{-1}, while no water flux is adjusted at the cathode side. The anode inlet flux temperature was controlled with a heated hose ($20°C \leq T \leq 80°C$), the temperatures at the anode and cathode outlet were measured with Pt100 sensors. The pressures at the anode and cathode inlets and outlets were monitored but did not exceed the ambient pressure appreciably. A LabView program monitored all sensors and controlled anode temperature and water flux.

Results and Discussion

In the following section segmented current density mapping and EIS measurement are used to characterize the cell voltage losses of a PEMWE cell. Therefore, one operation mode with a sufficient water flux is compared with an operation of an insufficiently low water flux. In the first section, the different current density distributions of these cases are investigated. Subsequently, the different polarization behaviors of these two modes are observed followed by an analysis of the cell voltage losses and their differences in the next subsection. Finally, local differences in the cell voltage losses are observed and discussed.

Current density distribution.—In a preliminary work the authors observed the influence of water flux rates on the current density distribution in PEMWE cells.[10] The stoichiometric water ratio λ was used to relate the adjusted inlet water flux of the anode to the amount of water consumed in the electrolysis reaction:

$$\lambda = f(i, \dot{m}) = \frac{\dot{m}_{in}^{A}}{\frac{i}{2F} \cdot \tilde{M}_{H_2O}} \quad [1]$$

Herein, $\dot{m}_{in}^{A}$ represents the active area specific water inlet flux on the anode side (in mg min^{-1} cm^{-2}; for water 1 mg corresponds to approximately 1 µL), $\tilde{M}_{H_2O}$ the molar mass of water and F the Faraday constant. The authors determined that the CDD is constant and quite homogeneous for stoichiometric water ratios of $\lambda \geq 10$ along the 50.4 cm cell. However, reduced stoichiometric water ratios of $\lambda \leq 5$ lead to a decrease in current density in the outlet region of the cell (Fig. 2). These results agree with the results of Sun et al.[8] with a smaller cell.

For the present analysis, the CDD was measured for an over-stoichiometric case, further called reference (ref.) case, with a specific water flux of $\dot{m}_{in}^{A} = 44$ mg min^{-1} cm^{-2} and a resulting $\lambda = 11$ (black line with circles in Fig. 2). Additionally, two experiments (galvanostatic and potentiostatic operation mode) were performed, in which the specific water flux was reduced to $\dot{m}_{in}^{A} = 18$ mg min^{-1} cm^{-2} (called dry case in the following). CDDs under dry and galvanostatic operation mode were used to verify the experiments with literature results.[8,10] Furthermore, CDDs under dry and potentiostatic operation mode were measured, which guarantees that the cell voltage is distributed homogeneously along the cell for the segmented and the unsegmented measurements. For the potentiostatic dry case (blue line with diamonds in Fig. 2) the cell voltage was adjusted similar to the

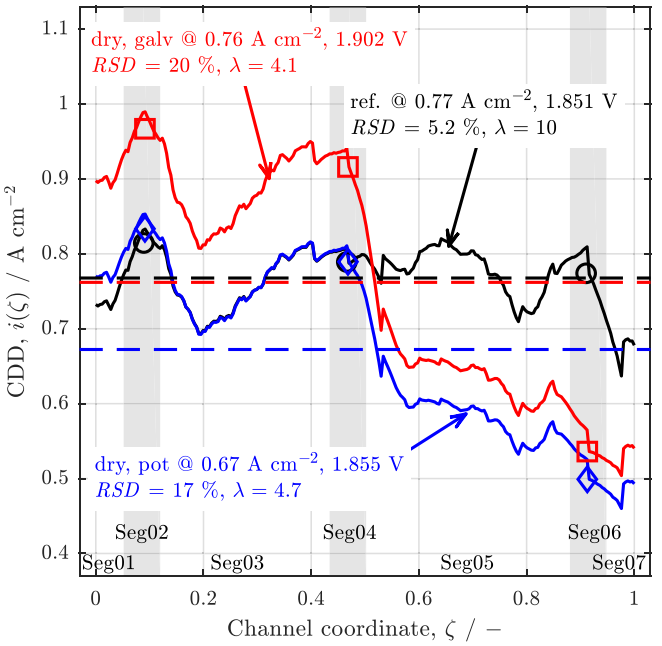

Figure 2. Along the channel current density distributions (CDDs), $i(\zeta)$ smoothed by moving averages (see Eq. A1) as solid lines; Dashed horizontal lines show mean current density $\bar{i}$; Reference case (ref) and two dry cases (dry) of either similar cell voltage ($U_{cell} \approx 1.85$ V) or similar mean current density ($\bar{i} \approx 0.76$ A cm^{-2}); Gray vertical stripes indicate location of the EIS measurement segments Seg02, Seg04, Seg06 with markers for local current density of each segment; *RSD* representing the relative standard deviation of each CDD.

reference case. For the galvanostatic dry case (red solid line with squares in Fig. 2) the integral current density was adjusted similar to the current density measured in the reference case. Table I summarizes the properties of the three CDD cases.

The CDD in the reference case shows a pronounced (±100 mA cm^{-2}) but stable fluctuation of the local current densities around its mean current density $\bar{i}^{ref}$ (dashed black line) indicated by a relative standard deviation (RSD) of $RSD^{ref} = 5.2\%$. Typically, this fluctuation is based on local contact resistances due to different local passivization or contacting of the PTL for instance.[10] In the potentiostatic mode of similar voltages (≈1.85 V) and with a reduced specific water flux, the CDD shows an almost congruent progression with the reference case along the first half of the channel, while the current density in the second half drops significantly. This leads to an integral reduction of the mean current density together with an increase of the overall RSD ($RSD^{dry,pot} = 17\%$). The stoichiometric water ratio as a function of mass flow and integral current density decreases to λ = 4.7. In the dry, galvanostatic operation mode the integral current density is adjusted similar to the reference case. As expected, the local current density drops at the down-stream part of the channel. Consequently, to maintain the integral current density the local current density at the inlet of the channel increases. The higher current at the cell inlet leads to an increase of the cell voltage by about 50 mV, a decrease of the CDD homogeneity ($RSD^{dry,galv} = 20\%$) and a descend of the stoichiometric water ratio to λ = 4.1.

Table I. Overview on the three different CDD cases.

Case	U_{cell} V	$\bar{i}$ A cm^{-2}	$\dot{m}_{in}^{A}$ mg min^{-1} cm^{-2}	λ -	*RSD* %
ref.	1.851	0.77	44	11	5.2
dry, pot.	1.855	0.67	18	4.7	17
dry, galv.	1.902	0.76	18	4.1	20

Polarization curve.—Polarization curves were measured potentiostatically for the reference and the dry case (specific water fluxes of $\dot{m}_{in}^{A} = 44$ mg min^{-1} cm^{-2} and $\dot{m}_{in}^{A} = 18$ mg min^{-1} cm^{-2}) to observe the effect of different water stoichiometries as a function of the current density. Fig. 3a shows the U/i-curves for the reference case. The circled black line represents the cell voltage over a summation of all local current densities, further called integral performance. The other three polarization curves represent the local performance at three characteristic positions along the channel coordinate, which is a well known representation for segmented fuel cell experiments.[1,15]

In the reference case, all polarization curves show the same qualitative behavior (Fig. 3a). The slightly better performance of the local polarization curves can be explained by minor current density differences between the investigated segments Seg02, Seg04, Seg06 and the full cell measurement (≈ ±10 mA cm^{-2}). For the highest adjusted cell potential of $U_{cell} = 2.05$ V a stoichiometric water ratio of λ = 6.1 is reached (see Eq. 1). This very low stoichiometric ratio leads to a lack of water in the very end of the channel indicated by the performance drop of Seg06 (see Fig. 3a-1).

This performance loss in the outlet region of the channel is highly intensified by a further reduction of the water flux. In the dry case, the voltage step from $U_{cell} = 1.775$ V to $U_{cell} = 1.80$ V (see Fig. 3b) reduces the local current density of Seg06 in the down-stream part of the channel by about $\Delta\bar{i} \approx 100$ mA cm^{-2}. In comparison to the reference case at $U_{cell} = 1.80$ V the local current density is reduced by $\Delta\bar{i} \approx 180$ mA cm^{-2}. This strong drop of current density in the outlet region is also coupled to a significant but less pronounced decrease of the integral cell performance. A further increase of the cell voltage strongly reduces the local performance of Seg06 and increases the integral performance losses represented by an increased progression of the polarization curve. In contrast, the polarization curve of the upstream part (Seg02) and the middle part (Seg04) show almost identical performance as in the reference case (≈ 1.0 A cm^{-2} resp. 0.9 A cm^{-2} at 1.9 V). For cell voltages above $U_{cell} = 1.95$ V the CDD drops also in the middle of the cell, which is indicated in the polarization curves by the strong performance loss in Seg04. Similar to Seg06, the middle segment initially shows a strong reduction in current density, followed by a convergence to a limiting current density for higher cell voltages.

These characteristic drops of the CDD at the channel outlet are also documented in literature for PEMFCs[16,17] and for electrochemical hydrogen compression.[18] In fuel cells the educt starvation at the outlet of the cell builds up a reaction front, which moves toward the inlet, when the amount of educt is further reduced. Mass transport limitation of oxygen in a PEMFC is considered as the main issue for that phenomenon. For a PEMWE cell, the principles of the performances losses at low stoichiometric water ratios are discussed in the following.

Cell voltage loss analysis.—The integral cell voltage U_{cell} can be divided into the sum of the thermodynamic cell voltage, $U_{th}^{0} = 1.195$ V (at 60°C, atmospheric pressure) and the following major overpotentials,

$$U_{cell} = U_{th}^{0} + \eta_{act} + \eta_{\Omega} + \eta_{mtx} \quad [2]$$

in which η_{act} represents the activation overpotential, η_{Ω} the Ohmic overpotential and η_{mtx} the mass transport overpotential. In the following, a systematic observation of the particular losses is conducted, to identify the processes that lead to the performance reduction at low stoichiometric water ratios.

Ohmic losses.—The high frequency resistances (HFRs) are measured at different current densities (see Fig. 4) to determine the impact of the Ohmic resistance on the performance differences between the reference and the dry case. The reference case shows a constantly decreasing HFR with increasing current density, which is almost linear above $\bar{i} = 0.1$ A cm^{-2}.

Generally, a decrease of the HFR with increasing current density can be caused by a temperature increase in the catalyst layer and the membrane due to the increasing waste heat production with

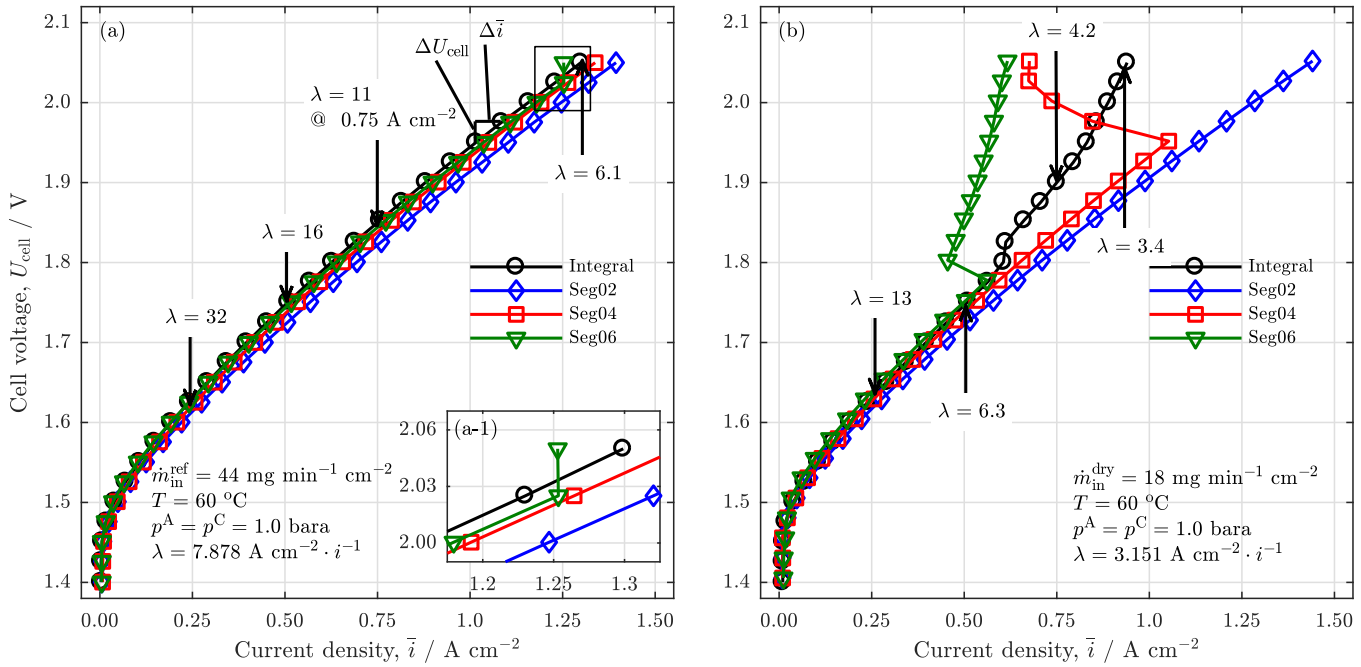

Figure 3. Polarization curves for the full cell and three representative cell segments in the front part of the channel, Seg02, the middle part, Seg04, and the oulet part, Seg06 at (a) the reference case with a water flux resulting in sufficient stoichiometric water ratios calculated with Eq. 1 (exemplary: $\lambda = 11$ at 0.75 A cm^{-2}); (a-1) inset for high voltages in the reference case; and at (b) the dry case with an insufficient water flux for current densities of $\bar{i} \geq 0.55$ A cm^{-2} (exemplary: $\lambda = 4.2$ at 0.75 A cm^{-2}); Holding time per voltage step $t = 300$ s.

increasing polarization.[19] The relation between membrane temperature and membrane resistance is empirically described by Springer et al.[20] for a Nafion117 membrane. However, with a constant temperature of $T = 60$°C in the anode and cathode end plates (adjusted by the external heating elements) and assuming that the membrane is fully hydrated ($\lambda_{mem} = 20$),[21] a temperature increase of $\Delta T = 10$°C in the membrane solely leads to a HFR reduction of $\Delta R_{HFR} = 13$ mΩ cm^2. Although a current density increase from $\bar{i} = 0.1$ A cm^{-2} to $\bar{i} = 1$ A cm^{-2} possibly exceeds the assumed temperature difference of $\Delta T = 10$°C, it is highly unlikely that only a temperature effect in the membrane and the electrode explains the strong HFR decrease of $\Delta R_{HFR} \approx 60$ mΩ cm^2.

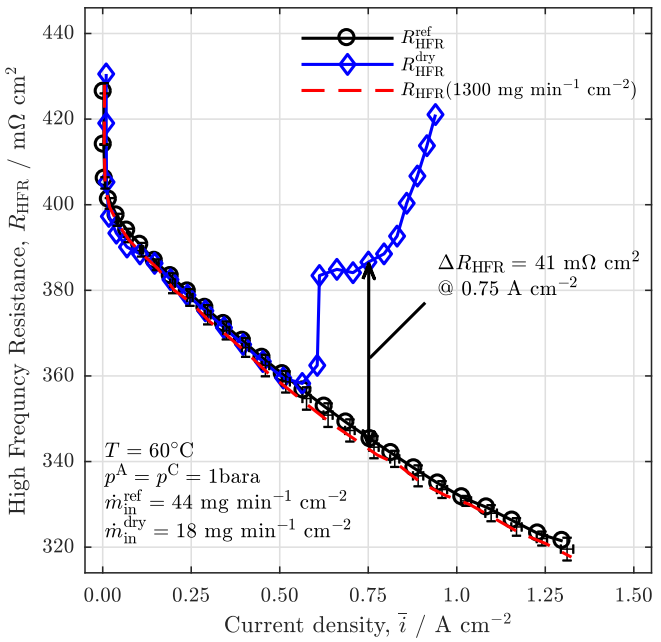

Figure 4. High frequency resistance (HFR) measurements of the integral cell at different current densities in the reference and the dry case. Error bars represent HFR trends of four adjusted water fluxes from 44 mg min^{-1} cm^{-2} to 1300 mg min^{-1} cm^{-2}. Dashed line shows the HFR trend for highest adjusted water flux corresponding to $\lambda \approx 235$ at 1.0 A cm^{-2}.

Nevertheless, Fig. 4 proves that this trend was reproducible with several mass flows from 44 mg min^{-1} cm^{-2} (see black line with circles) to 1300 mg min^{-1} cm^{-2} (see dashed red line), which is indicated by the errorbars. For a quantitative comparison with the dry case this decreasing trend of the HFR (black circle line) was defined as the reference case. Generally, the resistance of the setup is relatively high in comparison to the literature data for cells using Nafion117 membranes.[22] Though, the work of Verdin et al.[7] has shown that a similar *S++* setup exhibits even higher Ohmic resistances.

The HFRs of the dry case (blue diamond line in Fig. 4) were equivalent to the ones of the reference case for mean current densities of $\bar{i} \leq 0.5$ A cm^{-2}, which correspond to stoichiometric water fluxes of $\lambda \geq 6$. At $\bar{i} \approx 0.55$ A cm^{-2} a sharp increase in the HFR occurs, followed by a continuous growth of the Ohmic resistances for higher current densities. It can be hypothesized that the HFR is increasing due to the dehydration of the membrane, as it is directly proportional to its proton conductivity. A sufficient inlet flux simultaneously feeds the anode reaction, humidifies the membrane and compensates the net water drag 13 m/Ω cm^2 from anode to cathode. In contrast, an insufficient water flux is likely to lower the level of membrane humidity and consequently reduces the water flux through the membrane. This water flux can be described with the net drag coefficient n_g as the ratio of water molecules permeating through the membrane and to evolved protons. Net drag coefficients of $2 \leq n_g \leq 5$ are reported,[23,24] which can be added onto the feed water flux for the anode reaction. This allows to calculate the necessary minimal stoichiometric water ratio with $\lambda_{min} = 1 + 2 \cdot n_g = 5$, which is in the same order of magnitude of the herein observed critical stoichiometric water ratio of $\lambda \approx 5$.

With lower stoichiometric ratios all water in the anode is consumed by the reaction or crosses the membrane and cannot fully hydrate the membrane anymore. The dehydration of the membrane leads to a reduced proton mobility and can change the proton transport processes

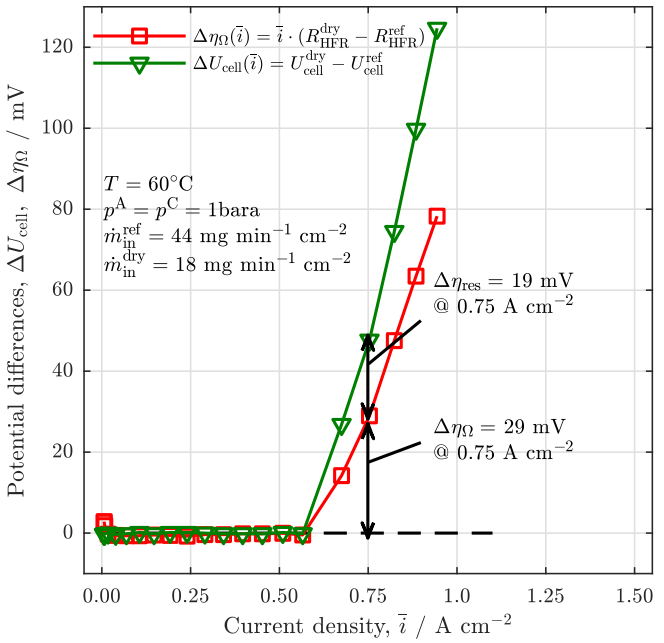

Figure 5. Differences of the Ohmic overpotential $\Delta\eta_\Omega$ and the cell voltage ΔU_{cell} between the reference and the dry case for the integral cell and the residual overpotential of $\Delta\eta_{\mathrm{res}} = \Delta U_{\mathrm{cell}} - \Delta\eta_\Omega$.

in the membrane.[25,26] Consequently, with a lower proton conductivity the membrane's Ohmic resistance increases.

The difference between the Ohmic overpotential in the reference and dry case ($\Delta\eta_\Omega = \bar{i} \cdot (R_{\mathrm{HFR}}^{\mathrm{dry}} - R_{\mathrm{HFR}}^{\mathrm{ref}})$) is presented in Fig. 5 (red line with squares) and quantifies the effect of the membrane dehydration. Additionally, Fig. 5 shows the difference between the overall cell voltages of the dry and the references cases obtained from the data in Figs. 3a,b (green lines with triangles). Although the difference in the Ohmic losses $\Delta\eta_\Omega$ strongly increase for current densities of $\bar{i} \geq 0.55$A cm^{-2}, a significantly higher cell voltage difference is observed. For a mean current density of $\bar{i} = 0.75$ A cm^2 the voltage increase related to a HFR increase is about 30 mV. However, a considerably higher overall cell voltage increase of about 50 mV is measured. Consequently, additional overpotential sources have to be considered.

Activation losses.—Fig. 6a shows the HFR-corrected cell voltage $U_{\mathrm{HFR-free}}$ as a function of the mean current density (logarithmic scale). As expected, in the region of low current densities (0.02 A cm^{-2} $\leq \bar{i} \leq$ 0.50 A cm^{-2}) both polarization curves show an excellent accordance, while for higher current densities the polarization curves deviate, similar to Fig. 5. (The divergences in the region of $\bar{i} \leq 0.01$ A cm^{-2} must be attributed to systematic measurement uncertainties.) The HFR-corrected polarization curves enable the examination of the activation overpotentials of the reference and the dry case in the absence of mass transport losses at small current densities. Based on the simplified Butler-Volmer equation, the empirical Tafel kinetic can be described with b as the Tafel slope in a form of

$$\eta_{\mathrm{act}} = b \cdot \log\left(\frac{i}{i_0}\right) \qquad [3]$$

Because the reaction kinetics of the hydrogen evolution reaction are much faster than these of the oxygen evolution reaction (OER),[27] the OER overpotential is equal to the activation overpotential ($\eta_{\mathrm{OER}} = \eta_{\mathrm{act}}$). For very low current densities (0.02 A cm^{-2} to 0.1 A cm^{-2}) the HFR-free polarization curves can be approximated linearly. The resulting Tafel lines correspond to Tafel slopes of $b^{\mathrm{ref}} \approx b^{\mathrm{dry}} \approx$ 50 mV dec^{-1} (similar to literature for IrO_x[28,29]).

The good accordance of both slopes indicates that the reaction kinetics do not change due to a reduction of the anode water flux. Therefore, the activation overpotential cannot explain the remaining performance losses, as long as a constant Tafel slope for all current densities is assumed. Consequently, the remaining cell voltage differences can be attributed to the mass tranport losses (see Fig. 6a and the inset Fig. 6a -1).

Table II. Comparison between the low frequency resistance, R_{LFR} and the slopes of the polarization curve, $R_{\mathrm{Ui}} = \Delta U_{\mathrm{cell}}/\Delta\bar{i}$ (see Fig. 3) for three mean current densities.

$\bar{i}$ A cm^2	$R_{\mathrm{Ui}}^{\mathrm{ref}}$ mΩ cm^2	$R_{\mathrm{LFR}}^{\mathrm{ref}}$ mΩ cm^2	$R_{\mathrm{Ui}}^{\mathrm{dry}}$ mΩ cm^2	$R_{\mathrm{LFR}}^{\mathrm{dry}}$ mΩ cm^2
0.25	511	500	507	495
0.50	439	427	457	427
0.75	392	392	568	-

Mass transport losses.—The difference between the extrapolated Tafel line and the HFR-corrected polarization curve represents the mass transport losses η_{mtx} (see Fig. 6). As expected, η_{mtx} increase with increasing $\bar{i}$. Exemplary, for $\bar{i} = 0.75$ A cm^{-2} the reference case shows voltage losses of $\eta_{\mathrm{mtx}}^{\mathrm{ref}} = 39$ mV. Literature results confirm this magnitude and reveal a pseudo-linear increase of the mass transport losses with the investigated current density range.[19,30,31] This linear increase was detected for the reference case but did not match for the dry case (see Fig. 6b). At current densities of $\bar{i} \geq 0.55$ A cm^{-2} the mass transport losses of the dry case show a significantly higher increase with current density compared to the reference case, with additional losses of 50% for $\bar{i} = 0.75$ A cm^{-2}, exemplary.

For a deeper analysis of the mass transport losses, EIS measurements were performed. In Figs. 6c,d the reference and dry case measurements are presented for three different current densities. For the lowest current density (black circles), the reference and the dry case each show one non-ideal semi-arc. With an increase of current, the arcs shrink and the HFR intercept is shifted left (blue diamonds). This behavior is consistent for all currents of the reference case and for the two spectra of lower current densities in the dry case. For all spectra no significant dehydration of the membrane takes place. Exemplary for $\bar{i} = 0.25$ A cm^{-2} both EIS spectra for the dry and the reference show similar behavior, indicating a similar membrane hydration for different stoichiometric water ratios, and an unchanged water transport through the PTL. This is supported by Seweryn et al.,[33] who have shown for different $\lambda \geq 1000$ that the water/gas ratio in the PTL is not affected by the stoichiometric water ratio.

All EIS spectra of the reference case and the two low current EIS spectra for the dry case show a second intercept of the x-axis for frequencies in the range of $f = 100$ mHz, at which the low frequency resistance (LFR) is obtained. The LFR intercept represents the sum of all Ohmic, activation and mass transfer resistances. Therefore, the LFR must correspond to the slope of the polarization curve at each individual operating point, which is calculated with the difference quotient ($R_{\mathrm{Ui}} = \Delta U_{\mathrm{cell}}/\Delta\bar{i}$). For all experiments without dehydration effects, the LFR and the slopes of the polarization show positive agreement with a difference of maximally 7% (see Table II and Fig. 3a), proving the consistency of the different measurement techniques.

For the highest current density in the dry case (red squares) the HFR intercept is shifted right and a second arc develops at frequencies ≤ 3.5 Hz. For this operation mode no LFR could be determined. While the right-shift of the HFR can be explained with the dehydration of the membrane, the phenomenological root of the second semi-arc is not fully understood yet.

Recently, Babic et al.[32] investigated the mass transport losses of three different sintered PTLs with different pore and particle sizes. They assume that the different PTL surfaces deform the catalyst layer at their interface resulting in different diffusion lengths for feed water, which is represented as a growing second semi-arc in the EIS spectra.

In the present work the formation of the second semi-arc in the EIS spectra is most likely caused by the lack of water in the catalyst layer in the downstream region of the cell. In comparison to

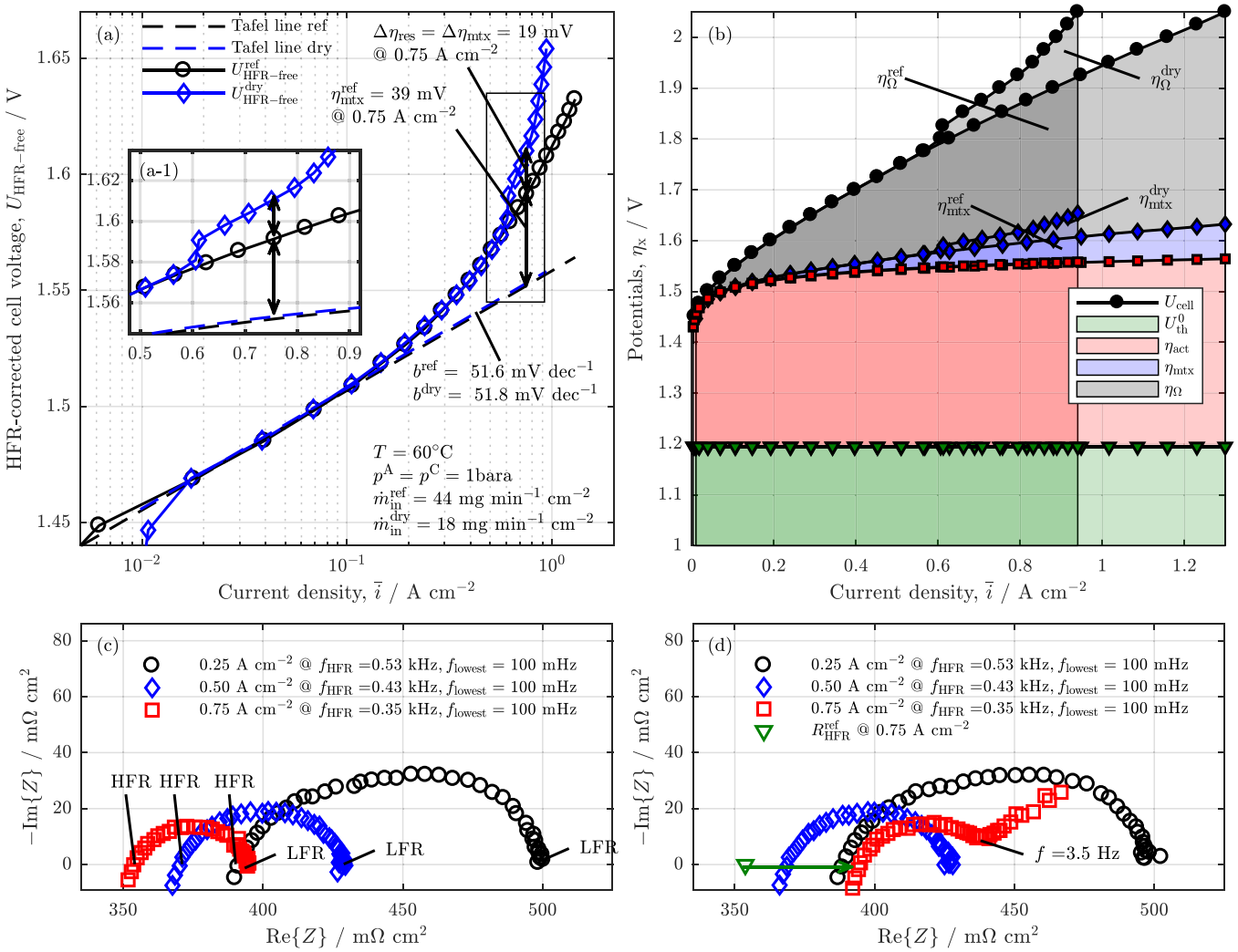

Figure 6. Cell voltage loss analysis with (a) the Tafel plot of the HFR-corrected cell voltage over current density; Inset (a-1) shows the drifting apart of both HFR-corrected curves in regions of higher current densities. (b) Full breakdown of the cell voltage U_{cell} into thermodynamic cell voltage (U^0_{th}), activation losses (η_{act}), mass transport losses (η_{mtx}) and Ohmic losses (η_{Ω}); (c) Nyquist plot for the reference case presented at different current densities; (d) Nyquist plot at same current densities for the dry case; All measurements performed with the full cell.

Babic et al.[32] the PTLs and the interfaces do not change, however mass transport losses are provoked. It is suggested that these mass transport losses manifest similarly as a growing second semi-arc in the EIS spectra, when the water transport processes are hindered.

Together with a decrease of the conductivity in the relatively thick membrane, low water stoichiometric ratio may also dehydrate the ionomer in the thin catalyst layer (CL). From fuel cell literature it is well-known that the protonic resistance of the CL is not represented in the HFR of an EIS spectra, but shows frequency dependent behavior. A high proton conductivity in the cathode CL of a PEMFC is dependent on a sufficiently high level of ionomer hydration of the electrode.[34,35] Neyerlin et al.[34] show that a decrease of the relative humidity in the PEMFC cathode from 100% to 60% leads to a dehydration of the CL ionomer. Exemplary, at 0.75 A cm^{-2}, the CL Ohmic resitances increases by $\Delta R^{C,CL}_{H^+} \approx 30\,\mathrm{m\Omega\ cm^2}$. A similar magnitude could be calculated in the observed PEMWE cell for the same current density. When the residual overpotential difference of $\Delta\eta_{res} = 19\,\mathrm{mV}$ (see Fig. 5) is fully attributed to a decrease in CL proton conductivity, a CL resistance difference can be calculated to $\Delta R^{A,CL}_{H^+} = \Delta\eta_{res}/\bar{i} = 25\,\mathrm{m\Omega\ cm^2}$. For higher current densities even higher protonic resistances can be calculated, which correspond to a reduced ionomer hydration.

Spatial distribution of losses.—Due to the unique cell geometry, the experiments were extended to a local analysis of the cell voltage losses. Fig. 7 shows the Nyquist plots for (a) the integral cell, and the three EIS measurement segments (b) in the front (Seg02), (c) in the middle (Seg04) and (d) in the end of the channel (Seg06). Two cell voltages ($U_{cell} = 1.55$ V and $U_{cell} = 1.70$ V) were chosen in a way that no relevant dehydration of the cell was possible. A third cell voltage of $U_{cell} = 1.85$ V leads to a strong increase in the cell resistances in Seg06 (see Fig. 3b), while for a forth cell voltage of $U_{cell} = 2.00$ V a strong cell resistance increase and a performance loss can be observed in Seg06 and additionally in Seg04.

For cell voltages of $U_{cell} = 1.55$ V and $U_{cell} = 1.70$ V the Nyquist plots of the total cell (see Fig. 7a) show the characteristic trend as observed before. The HFR intercept slightly decreases with higher cell voltages and the semi-arc shrinks. At a cell voltage of $U_{cell} = 1.85$ V the dehydration of the membrane and the catalyst layer kicks in because of a critically low stoichiometric water ratio. The HFR increases and a second semi-arc occurs at lower frequencies. These two effects intensify at the highest voltage ($U_{cell} = 2.00$ V). Furthermore, the measurement becomes more sensitive at frequencies of $f \leq 1$ Hz.

The EIS spectra of Seg02 (Fig. 7b) indicate that the reduced stoichiometric water ratio ($\lambda \leq 5$) does not lead to a uniform dehydration of the membrane and the anode catalyst layer. Instead, the spectra

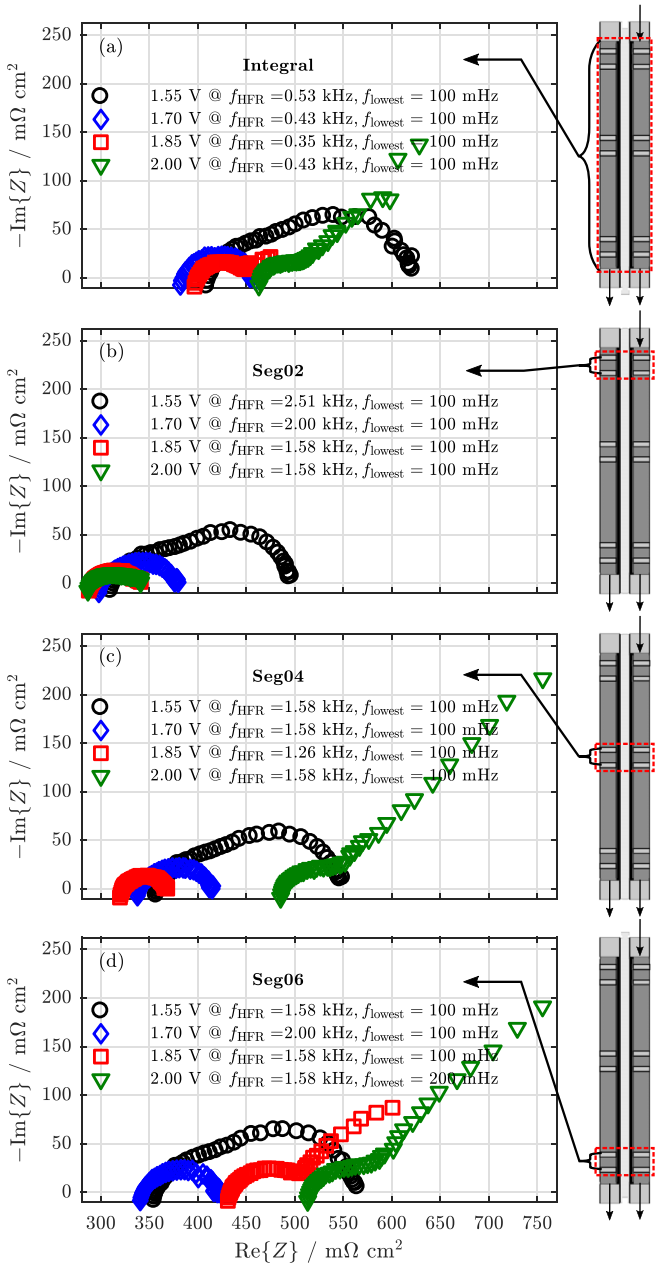

Figure 7. Spatially resolved potentiostatic EIS measurement at different cell voltages for low water flux of $\dot{m}_{in}^{A} = 18$ mg min^{-1} cm^{-2}: Nyquist plot for (a) the integral cell, (b) the segment at the channel inlet (Seg02), (c) the segment in the middle of the channel (Seg04) and (d) the segment at the outlet region of the channel (Seg06); HFRs and LFRs are shown in Table III; Temperature controlled to $T = 60°C$ at ambient pressure.

show the typical shrinking of the semi-arcs and a slight improvement of the HFRs with increasing cell voltages in the front region of the cell, where a sufficient amount of water is still present. The data confirm the observations from the CDD (Fig. 2) and the polarization curves discussed above (Fig. 3). The channel front is not affected in case of an integrally dehydration of the cell at low stoichiometric water ratios, due to the locally distributed hydration which decreases along the channel.

Furthermore, the hypothesis of a spatially distributed CCM hydration is supported by the EIS spectra for Seg04 and Seg06 (Figs. 7c,d). For $U_{cell} = 1.85$ V, Seg06 shows a similar EIS spectrum in comparison to the integral cell. A second semi-arc is formed and the HFR

Table III. Local HFR and LFR intercepts for the four cell voltages from Fig. 7.

U_{cell} V		Full Cell mΩ cm^2	Seg02 mΩ cm^2	Seg04 mΩ cm^2	Seg06 mΩ cm^2
1.55	HFR	412	312	359	357
1.70		384	301	339	343
1.85		399	290	322	433
2.00		465	290	488	516
1.55	LFR	621	496	549	564
1.70		455	380	415	422
1.85		–	341	368	–
2.00		–	341	–	–

increases. However, the HFR increase in Seg06 is significantly higher than the HFR increase of the integral cell (see Table III). For the highest adjusted cell voltage of $U_{cell} = 2.00$ V a strong HFR increase and the formation of a second semi-arc is also detected for Seg04. Solely Seg02 in the inlet part of the cell still does not show any obvious indications of dehydration.

The results of the local EIS measurements enable a qualitative estimation of the local hydration levels along the cell. The overall measurement of the polarization curve and the EIS spectra represent solely the averaged decrease of the cell's performance caused by a lack of water in the system. This shows that the local grade of dehydration might already be critical in the outlet region of the channel, while a full cell measurement would only reveal minor performance losses.

Conclusions

A segmented 50 cm single-channel cell was used to measure the cell performance, the current density distribution and the local electrochemical impedance spectra to analyze the observed performance loss phenomena locally distributed. Medium and low water fluxes were adjusted to observe the effects of decreasing stoichiometric water ratios on performance. Although low stoichiometric water ratios are not state of the art for conventional PEMWE cells, the authors have shown that stoichiometric water fluxes of $\lambda \geq 10$ allow a nearly undisturbed electrochemical operation of a PEMWE cell, under isothermal conditions. This potentially enables the reduction of mechanical energy for the anode water circulation and reduces the size of the water purification system, which could be of particular interest when aiming to the MW-scale PEMWE systems and the optimization of investment and operating costs.

It can be highlighted that a stoichiometric water ratio below $\lambda \approx 5$ leads to the dehydration of the anode catalyst layer and the membrane. EIS spectra for sufficient and insufficient water fluxes were carried out, which have shown i) an increase of the Ohmic resistances reflected in higher HFRs, due to a dehydration of the membrane and ii) the increase of the protonic resistance of the inonomer phase within the catalyst layer due to water transport limitations, which are represented by the formation of a transport semi-arc in the corresponding EIS spectra. The local current density mapping together with the local EIS measurement revealed that the dehydration of the CCM differs locally with the most pronounced dehydration at the outlet region of the cell.

The results indicate that a local and temporary dehydration of the CCM can be reversible on a short time scale in the range of several seconds or minutes. However, a permanent but also fluctuating dehydration of the CCM can potentially serve as an unfavored stressor or accelerator for membrane and catalyst degradation rates. On the other hand, cleverly designed dehydration experiments can potentially serve as accelerated stress tests for the CCM.

Acknowledgments

Financial support by the German Research Foundation (Deutsche Forschungsgemeinschaft, DFG) within the framework of the project grant HA 6841/2-1 is gratefully acknowledged.

Appendix

For a better visualization, the current density profiles in Fig. 2 are smoothed by a moving average. In the following equation the averaging is described

$$i(k) = \begin{cases} \dfrac{i(1) + \cdots + i(k) + \cdots + i(k+7)}{k+7} & \text{for } k \leq 8 \\ \dfrac{i(k-8) + \cdots + i(k) + \cdots + i(k+7)}{16} & \text{for } 9 \leq k \leq 245 \\ \dfrac{i(k-8) + \cdots + i(k) + \cdots + i(252)}{252 - k + 9} & \text{for } k \geq 246 \end{cases} \quad [A1]$$

with k as the consecutive number for each current density measurement segment ($k \in \mathbb{N}$, $k = [1, 252]$).

ORCID

C. Immerz https://orcid.org/0000-0001-9163-0240
B. Bensmann https://orcid.org/0000-0001-8685-7192
P. Trinke https://orcid.org/0000-0002-0935-5321
M. Suermann https://orcid.org/0000-0001-9685-7081

References

1. S. J. C. Cleghorn, C. R. Derouin, M. S. Wilson, and S. Gottesfeld, *J. Appl. Electrochem.*, **28**(7), 663 (1998).
2. A. Phillips, M. Ulsh, J. Porter, and G. Bender, *Fuel Cells*, **17**(3), 288 (2017).
3. S. Herden, F. Riewald, J. A. Hirschfeld, and M. Perchthaler, *J. Power Sources*, **355**, 36 (2017).
4. Y. Zhang, A. Smirnova, A. Verma, and R. Pitchumani, *J. Power Sources*, **291**, 46 (2015).
5. S. Kirsch, R. Hanke-Rauschenbach, B. Stein, R. Kraume, and K. Sundmacher, *J. Electrochem. Soc.*, **160**(4), F436 (2013).
6. J. A. Nogueira, I. K. P. Arias, R. Hanke-Rauschenbach, T. Vidakovic-Koch, H. Varela, and K. Sundmacher, *Electrochim. Acta*, **212** (2016).
7. B. Verdin, F. Fouda-Onana, S. Germe, G. Serre, P. Jacques, and P. Millet, *Int. J. Hydrogen Energy*, **42**(41) (2017).
8. S. Sun, Y. Xiao, D. Liang, Z. Shao, H. Yu, M. Hou, and B. Yi, *RSC Adv.*, **5**, 14506 (2015).
9. I. Dedigama, P. Angeli, N. van Dijk, J. Millichamp, D. Tsaoulidis, P. Shearing, and D. Brett, *J. Power Sources*, **265**, 97 (2014).
10. C. Immerz, M. Schweins, P. Trinke, B. Bensmann, M. Paidar, T. Bystron, K. Bouzek, and R. Hanke-Rauschenbach, *Electrochim. Acta*, **260**, 582 (2018).
11. A. C. Olesen, C. Rømer, and S. K. Kær, *Int. J. Hydrogen Energy*, **41**(1), 52 (2016).
12. B. Bensmann, R. Hanke-Rauschenbach, I. Peña Arias, and K. Sundmacher, *Electrochim. Acta*, **110**, 570 (2013).
13. U. Babic, M. Suermann, F. N. Büchi, L. Gubler, and T. J. Schmidt, *J. Electrochem. Soc.*, **164**(4), F387 (2017).
14. D. J. Brett, S. Atkins, N. P. Brandon, V. Vesovic, N. Vasileiadis, and A. R. Kucernak, *Electrochem. Commun.*, **3**(11), 628 (2001).
15. M. M. Mench and C. Y. Wang, *J. Electrochem. Soc.*, **150**(1), A79 (2003).
16. M. M. Mench, C. Y. Wang, and M. Ishikawa, *J. Electrochem. Soc.*, **150**(8), A1052 (2003).
17. N. Zamel, R. Hanke-Rauschenbach, S. Kirsch, A. Bhattarai, and D. Gerteisen, *Int. J. Hydrogen Energy*, **38**(35), 15318 (2013).
18. M. Suermann, T. Kiupel, T. J. Schmidt, and F. N. Büchi, *J. Electrochem. Soc.*, **164**(12), F1187 (2017).
19. M. Suermann, T. J. Schmidt, and F. N. Büchi, *Electrochim. Acta*, **211**, 989 (2016).
20. T. E. Springer, T. A. Zawodzinski, and S. Gottesfeld, *J. Electrochem. Soc.*, **138**(8), 2334 (1991).
21. K.-D. Kreuer, *Solid State Ionics*, **252**, 93 (2013).
22. I. Radev, G. Georgiev, V. Sinigersky, and E. Slavcheva, *Int. J. Hydrogen Energy*, **33**(18), 4849 (2008).
23. K. Onda, T. Murakami, T. Hikosaka, M. Kobayashi, R. Notu, and K. Ito, *J. Electrochem. Soc.*, **149**(8), A1069 (2002).
24. P. Medina and M. Santarelli, *Int. J. Hydrogen Energy*, **35**(11), 5173 (2010).
25. A. M. Pivovar and B. S. Pivovar, *J. Phys. Chem. B*, **109**(2), 785 (2005).
26. R. Devanathan, A. Venkatnathan, and M. Dupuis, *J. Phys. Chem. B*, **111**(28), 8069 (2007).
27. J. Durst, A. Siebel, C. Simon, F. Hasch, J. Herranz, and H. A. Gasteiger, *Energ. Environ. Sci.*, **7**(7), 2255 (2014).
28. M. Bernt and H. A. Gasteiger, *J. Electrochem. Soc.*, **163**(11), F3179 (2016).
29. M. Bernt, A. Siebel, and H. A. Gasteiger, *J. Electrochem. Soc.*, **165**(5), F305 (2018).
30. M. Suermann, K. Takanohashi, A. Lamibrac, T. J. Schmidt, and F. N. Büchi, *J. Electrochem. Soc.*, **164**(9), F973 (2017).
31. A. Nouri-Khorasani, E. T. Ojong, T. Smolinka, and D. P. Wilkinson, *Int. J. Hydrogen Energy*, **42**(48), 28665 (2017).
32. U. Babic, T. J. Schmidt, and L. Gubler, *J. Electrochem. Soc.*, **165**(15), J3016 (2018).
33. J. Seweryn, J. Biesdorf, T. J. Schmidt, and P. Boillat, *J. Electrochem. Soc.*, **163**(11), F3009 (2016).
34. K. C. Neyerlin, W. Gu, J. Jorne, A. Clark, and H. A. Gasteiger, *J. Electrochem. Soc.*, **154**(2), B279 (2007).
35. Y. Liu, M. W. Murphy, D. R. Baker, W. Gu, C. Ji, J. Jorne, and H. A. Gasteiger, *J. Electrochem. Soc.*, **156**(8), B970 (2009).